COGEAR

MODULE 3:

Modeling of slope behavior
Del. No.: 3b.2.6.1

Authors: Moore J.[1], Gischig V.[1], Burjanek J.[2], Löw S.[1], and Fäh D.[2]

[1] Engineering Geology, ETH Zürich
&
[2] Swiss Seismological Service

July 12, 2012

Task 3b.2.6

Modeling of slope behavior

Deliverable: 3b.2.6.1

Jeffrey Moore[1], Valentin Gischig[1], Jan Burjanek[2], Simon Loew[1], and Donat Fäh[2]

[1] Department of Earth Sciences, ETH Zurich

[2] Swiss Seismological Service, ETH Zurich

Summary

We evaluate the dynamic response of the large (~5 million m^3) unstable rock slope at Randa, Switzerland based on ground motion recordings during small earthquakes. Seismic measurements revealed strong polarization of the wavefield in the direction of maximum slope displacement, with spectral amplification factors ~5 within the unstable area. Results further highlighted resonant frequencies of both the large unstable rock mass and of individual blocks within it. Block vibration was confirmed by phase analysis of in-situ displacement measurements from two bounding tension fractures during a small earthquake. Numerical simulation using a discontinuous elastic model showed that the presence of steeply-dipping compliant fractures is crucial for recreating the observed site response. Such fractures are common in rock slope instabilities and are here shown to contribute to polarization and amplification of seismic shaking, site effects that are rarely considered for hard rock slopes and which may influence the potential for earthquake-triggered failure.

Citation

Introduction

The potential for an earthquake to trigger deep rock slope failure is controlled by both the degree of slope stability and shaking intensity at the site. Shaking intensity is, in turn, set by properties of the earthquake source and path (e.g., magnitude, epicentral distance, focal depth) and by modifications of the wavefield by site effects. Topographic amplification is commonly implicated as a source of augmented ground motion in steep terrain, and can be important in controlling the distribution of at least shallow slope failures (e.g., Sepúlveda *et al.,* 2005). However, expected maximum amplifications are typically around 50%. Other possible sources of amplification due to local site effects may play a more significant role in modifying the shaking intensity field in certain geological configurations (Spudich *et al.,* 1996; Ashford *et al.,* 1997).

Site response related to near-surface geological contrasts is typically analyzed for unconsolidated soil deposits overlying bedrock, and depends on seismic impedance contrasts and the depth of the basement. Many examples attest to amplified shaking, changes in frequency content, and wave trapping in basins due to site response (e.g., Baise *et al.,* 2003). In rock, however, site effects are generally not considered, even though strong impedance contrasts may arise due to near-surface weathering or zones of variable fracture density, and notable ground motion amplification has been observed

(e.g., Yoshimoto *et al.*, 1993; Steidl *et al.*, 1996). Concerning rock slope instabilities, Havenith *et al.* (2002) highlighted amplification caused by a near-surface layer of weathered rock as a key factor contributing to triggering of a historical rockslide in Kyrgyzstan. Similarly, Bozzano *et al.* (2011) describe the importance of jointed bedrock creating impedance contrasts and site amplification for a historical earthquake-triggered rock avalanche in Italy. Del Gaudio and Wasowski (2007) also discuss the combined role of both topographic and geological controls on directional variations in shaking intensity for landslide-prone slopes in Italy.

In this report, we describe combined investigations of the dynamic response of a large, active rock slope instability. Field measurements revealed strong amplification and polarization of the wavefield within the unstable rock mass, and highlighted resonant frequencies of blocks bounded by discontinuities. Block vibration was verified by in-situ strain measurements across two adjacent tension fractures during a nearby small earthquake. Numerical simulation was able to reproduce key features of the observed response simply by including a set of steeply-dipping, compliant tension fractures mapped at the site. Such fractures are common in active slope instabilities, and here we discuss their role in generating local site effects.

Randa Rock Slope Instability

The region of the Randa rockslide in canton Valais has the highest seismic activity in Switzerland and some of the greatest relief in the Alps. Magnitude (M_W) 6 or larger earthquakes have an average return period of 100 years (Fäh *et al.*, 2011) and invariably generate landslides. For example, the most recent major earthquake and its aftershocks (1946 Sierre, M_W 6.1) triggered a number of failures within the epicentral region and one large (~5 million m^3) rock avalanche (Fritsche and Fäh, 2009). Similarly, widespread rockfall was described during the 1855 M_W 6.4 earthquake near St. Niklaus in the Matter Valley (Fritsche *et al.,* 2006), near the Randa study site.

The current Randa rock slope instability is the legacy of two catastrophic failures in April and May 1991. Around 5 million m^3 of layered paragneiss and schists remain unstable today (the upper half of the 1991 failure scarp), moving at rates up to 20 mm/yr (Figure 1) (Gischig *et al.,* 2011). Underlying this unstable rock mass, a steep orthogneiss cliff shows no ongoing deformation after being exposed by the 1991 failures. Previous research at the site provided detailed information on the internal structure and kinematics of the unstable rock mass from integrated measurements. These included surface fracture mapping and borehole logging (Willenberg *et al.,* 2008), 3D seismic refraction tomography (Heincke *et al.,* 2006), and 3D surface and borehole georadar (Spillmann, Maurer, Willenberg, *et al.,* 2007). Borehole logging and surface measurements revealed active fracture zones and their relative displacement rates. A series of steeply-dipping fractures could be traced from the surface to ~80 m depth with geophysical imaging to where the fractures intersected a borehole. Large-scale discontinuities delineate blocks, which combine to form compartments in the upper area of the instability. These compartments (or meso-scale block assemblages) have been shown through high-resolution geodetic surveying to move at similar rates and orientations (see Gischig *et al.,* 2011). Toppling was identified as the dominant failure mode in the upper part of the instability, while translational sliding on a stepped failure surface was postulated in the lower area.

Our study builds on previous experiments at the Randa slope instability with the goal of describing the dynamic response of the unstable rock mass. Data sets used include analysis of regional earthquakes recorded previously by a micro-seismic monitoring array, analysis of new seismic data from two seismometers located inside and outside of the unstable rock mass, and in-situ measurements of coseismic strain across two tension

cracks during a nearby small earthquake. Previously published ambient vibration measurements (Burjanek *et al.,* 2010) are also briefly summarized and incorporated.

Results

Ambient Vibration Analysis of Noise

Ambient vibration measurements were conducted in summer 2008 and presented by Burjanek *et al.* (2010). Site-to-reference spectral ratios were calculated for 33 stations within and outside of the unstable rock mass. Spectral ratios compare the frequency-dependent station response to that of a reference station on nearby stable ground. Results showed strong amplification within the instability, with spectral ratios up to 5 at 3 Hz and up to 10 at 5 Hz (Figures 2a and 2b). The boundary of the amplified area coincided closely with the boundary of the unstable rock mass. Polarization analysis revealed that the wavefield within the instability is strongly polarized in the direction of maximum slope displacement (azimuth ~135°, slight upward dip angle). No amplification or polarization was observed outside the unstable area. Measurements suggested that the wavefield within the instability may be controlled by normal mode vibration of individual blocks, superimposed on that of the large unstable volume.

Response to Small Regional Earthquakes

Nearly 80 regional earthquakes were recorded by a network of nine 8 Hz, 3-component geophones deployed at the site between 2002 and 2004 (for specifications see Spillmann, Maurer, Green, *et al.*, 2007). These earthquakes were small, with typical local magnitudes M_L ~0.5–2 at epicentral distances of 10–40 km. The geophone array was distributed around the site in shallow (2–4 m) boreholes inside and outside of the unstable rock mass. Site-to-reference spectral ratios were calculated (as in Burjanek *et al.,* 2010) and are presented in Figures 2c and 2d resolved at an azimuth of 135°. Results show notable amplification within the instability with mean spectral ratios up to ~5, similar to ambient noise results. Many stations in the unstable area showed spectral peaks at ~3 Hz. Amplification was found to be greatest in the region of maximum instability thickness.

Seven additional earthquakes were recorded by two 5 sec seismometers deployed in summer 2009 (RAND1 and RAND2, Figure 2c). Earthquake magnitudes were again small, M_L ~0.6–1.5 at epicentral distances of 20–40 km. Site-to-reference spectral ratios (at 135° azimuth) are in good agreement with previously recorded data. Mean amplifications within the unstable area reached factors of nearly 7 for a frequency band centered around 3 Hz (Figures 2c and 2d), and another local spectral peak was identified at ~28 Hz.

Fiber optic strain sensors were installed at Randa in 2008 to measure coseismic deformation across key discontinuities both at the surface and at depth (Moore *et al.,* 2010). These fiber Bragg grating sensors can resolve micrometer-scale displacements at 100 Hz triggered sampling. In May 2010, an earthquake of M_W 3.2 occurred about 5 km north of Randa at a focal depth of ~5 km. Data from the two surface crack extensometers (Cracks Z9 and Z10; about 20 m apart) are presented in Figure 3, along with ground motion from the nearest seismic station EMBD ~5 km from the epicenter. Note that the time axes are not absolute, since the two systems are not precisely synchronized. Peak amplitude of induced fracture displacements reached ~50 μm, while no significant permanent offset was recorded. Also shown in Figure 3 are spectra for both the displacement recordings and earthquake seismograms. Seismograms contain energy between 1 and 8 Hz, as well as two higher-frequency peaks at 14 and 17 Hz. Crack measurements show more distinct peaks at ~3 and 5 Hz. Narrow band-pass filtering of displacement signals revealed that the 3 Hz components for both tension

fractures are in-phase, while 5 Hz signals are out-of-phase. Borehole sensors did not record any observable transient displacements.

Discussion

Interpretation of Field Data

Analysis of ambient noise and earthquake recordings revealed strong amplification and polarization of the wavefield within the unstable rock mass at Randa. Polarization was most pronounced in the direction of slope movement, and site-to-reference spectral ratios showed amplifications typically around five. No polarization or amplification was observed outside the unstable area. The origin of this site response is intimately tied to the geological setting. Rock slope deformation results in preferential opening of tension fractures striking sub-perpendicular to the main displacement direction, allowing block vibration and creating meso-scale heterogeneity in rock mass moduli. At Randa, such fractures can be open by as much as ~1 m at the ground surface, where they are usually filled with collapsed colluvium and have minimum mapped vertical persistence of 80 m. Kinematic freedom required to allow block movement is provided by these steeply-dipping compliant fractures. Thus significant site effects can be observed in the unstable rock volume at Randa caused by preferential fracture opening, which can amplify ground motion by up to a factor of five. Similar site effects in rock slopes are rarely described in literature and are not commonly considered for earthquake triggering of deep slope instabilities; exceptions include e.g., Bozzano *et al.* (2011) who analyzed the role of rock fractures in a numerical study, and Havenith *et al.* (2002) who highlighted the influence of near-surface weathered rock. Important to note is that all measurements used in our analysis come from only weak ground motions and thus do not include any potential non-linear response.

Combined analysis of seismic recordings and transient displacements revealed resonant frequencies related to normal mode vibration of both the entire unstable rock volume and certain individual blocks within it. Most seismic stations within the unstable area showed spectral peaks at ~3 Hz, polarized in the main direction of active rock slope movement. However, higher-frequency peaks were also observed, which in some cases could be related to local rock blocks separated by open fractures. Similarly, coseismic crack displacement recordings showed two spectral peaks at ~3 and 5 Hz. The 5 Hz component of the signals was found to be out-of-phase, as expected for a block vibrating between the two sensors. Ambient noise measurements from the block between the two cracks also showed spectral peaks at 5 Hz (compare Figures 2a and 2b). Meanwhile, 3 Hz displacement signals were found to be in-phase, which likely represents the resonant frequency of the larger underlying unstable rock mass. Normal mode vibration of an unstable rock column was also recently described by Lévy *et al.* (2010), who reported progressive decrease in resonant frequency as a result of rock bridge failure prior to collapse. Changes in frequency were correlated with temperature, rainfall and freezing events, which affected the bulk modulus of the column. At Randa we could not identify any temporal changes in resonant frequency, although we were limited by a short time series of continuous seismic data.

Numerical Simulation

A numerical study of the Randa rock slope instability was conducted in UDEC (Universal Distinct Element Code; Itasca International Inc.) in an attempt to replicate key features of the observed dynamic response and identify controlling variables. In order to keep modeling and interpretation as simple as possible, we included only steeply-dipping opening-mode discontinuities mapped at the site in the area of our measurements (compare Figures 1b and 1c). Here we focus on the elastic response of the unstable rock mass and do not allow or attempt to predict slope failure. Instead, we assigned relevant

discontinuities high compliance values, which allows them to deform creating kinematic freedom and amplifying ground motion.

Figure 1c shows detail of the model geometry and material properties, which were adapted from a more complex geological and numerical model (Gischig *et al.,* 2011). Elastic rock mass properties correspond to seismic velocities of *Vp* = 3460 m/s and *Vs* = 2100 m/s, which are in accordance with results of Heincke *et al.* (2006). Discontinuity stiffness was varied in our model such that discontinuities simulating tension fractures had low shear and normal stiffness values of 0.1 GPa/m, while all other discontinuities had very high stiffness (100 GPa/m). Viscous boundary conditions were applied at the model sides, which absorb incoming seismic waves (although not perfectly at high incidence angles). A velocity boundary condition was implemented at the model base using the time history of the May 2010 earthquake recorded at the seismic station EMBD (Figure 3b). The EW- and Z-component of the seismogram were used as horizontal and vertical velocities, respectively, to generate a vertically-propagating wave. The mesh size of the model was at maximum 15 m; wavelengths larger than 200 m can be properly represented, while wavelengths shorter than 40 m result in aliasing. Therefore, frequencies below ~10 Hz are well-sampled, frequencies below ~50 Hz are not affected by aliasing, and we filtered the input seismogram with a 15 Hz low-pass filter. Rayleigh damping ensuring numerical stability was set to 0.1%. While the model and applied seismic loading are a simplified version of the true case, key features of the observed site response could be replicated.

Figure 4a compares average spectra for five stations located both inside and outside the unstable area (for monitoring points see Figure 1c). Also shown is the ratio of these mean spectra, which represents the modeled amplification within the instability compared to adjacent stable ground (Figure 4b). Amplification factors are greater than 1 throughout the frequency band and reach up to ~8 at 3 Hz. For comparison, we also conducted a simulation where discontinuity stiffness for all sets was set to high values in order to prevent relative displacements. For the latter 'stiff' model, spectral amplitudes from both inside and outside the slope instability are similar, and amplification factors vary around unity (Figure 4b). Thus, observed spectral amplification within the unstable rock mass at Randa could be replicated simply by including a set of steeply-dipping compliant fractures mapped at the site. Such fractures are common within actively-deforming rock slope instabilities such as Randa; compliance is assured by their wide aperture and unconsolidated material infilling.

Figure 4c shows modeled relative displacement across two fractures near the back of the slope instability (see Figure 1c) simulating the two monitored tension cracks; corresponding spectra are shown in Figure 4d. Amplitudes of the modeled signals are in good agreement with measured values (compare to Figure 3a), but the modeled waveforms exhibit a longer coda due to insufficient energy absorption at the boundaries. Similar to the measurements, modeled spectra contain peaks at around 2-3 and 4.5 Hz (compare to Figure 3b). Applying a narrow band-pass filter to these two frequency ranges revealed that modeled fracture displacements are nearly in-phase at 2-3 Hz and out-of-phase at 4.5 Hz. Especially Crack 1, which separates the stable and unstable areas, shows a clear 3 Hz spectral peak. Results can vary depending on the assumed depth and stiffness of the cracks; for deeper fractures frequencies drop and crack opening increases, while changes in stiffness are inversely related to modeled fracture displacement. Other parameters are constrained by field measurements. Overall, the results successfully reproduce fundamentals of the measured fracture displacement signals in terms of both amplitude and frequency content. Blocks are allowed freedom to vibrate simply by imposing low discontinuity stiffness. For greater stiffness values, predicted fracture displacements were orders of magnitude smaller than observed.

Conclusions and Outlook

Site effects are not typically considered for earthquake triggering of deep rock slope failures, however our measurements at Randa suggest that preferential fracturing of the rock mass within an active slope instability can locally amplify ground motion by factors of up to ten (for weak motions). We measured both significant spectral amplification and polarization of the wavefield within the unstable rock mass, which we could relate through numerical modeling to the presence of steeply-dipping compliant fractures. Rock slope movement results in opening of fractures striking sub-perpendicular to the main displacement direction, allowing block vibration and creating meso-scale heterogeneity in rock mass moduli. From a different perspective, we also point out that another source of rock fracturing – previous earthquakes – can result in systematic damage to rock slopes, which may in turn amplify local shaking intensity during subsequent earthquakes. Slope cracking from strong earthquakes is frequently observed (e.g., Petley *et al.,* 2006) and may be especially prevalent near ridge crests or slope breaks due to topographic amplification. Our results suggest a potentially important feedback between strong earthquakes, induced fracturing, and amplified shaking during later events, which combined with the reduced factor of safety of damaged slopes may increase the likelihood of subsequent earthquake-triggered failure.

Acknowledgments

References

Ashford, S.A., N. Sitar, J. Lysmer, and N. Deng (1997). Topographic effects on the seismic response of steep slopes, *Bull. Seismol. Soc. Am.,* **87**, 701-709.

Baise, L.G., S.D. Glaser, and D. Dreger (2003). Site response at Treasure and Yerba Buena Islands, California, *J. Geotech. Geoenviron.* **129**, 415-426.

Bozzano, F., L. Lenti, S. Martino, A. Montagna, and A. Paciello (2011). Earthquake triggering of landslides in highly jointed rock masses: reconstruction of the 1783 Scilla rock avalanche (Italy), *Geomorphology* **129**, 294-308.

Burjanek, J., G. Stamm, V. Poggi, J.R. Moore, and D. Fäh (2010). Ambient vibration analysis of an unstable mountain slope, *Geophys. J. Int.* **180**, 820-828.

Del Gaudio, V., and J. Wasowski (2007). Directivity of slope dynamic response to seismic shaking, *Geophys. Res. Lett.* **34**, L12301, doi:10.1029/2007GL029842.

Fäh, D., D. Giardini, P. Kästli, N. Deichmann, M. Gisler, G. Schwarz-Zanetti, S. Alvarez-Rubio, S. Sellami, B. Edwards, B. Allmann, F. Bethmann, J. Wössner, G. Gassner-Stamm, S. Fritsche, and D. Eberhard (2011). *ECOS-09 Earthquake Catalogue of Switzerland Release 2011. Report and Database. Public catalogue, 17.4.2011.* Swiss Seismological Service ETH Zürich, Report SED/RISK/R/001/20110417.

Fritsche, S. and D. Fäh (2009). The 1946 magnitude 6.1 earthquake in the Valais: site-effects as a contributor to the damage, *Swiss J. Geosci.* **102**, 423-439.

Fritsche, S., D. Fäh, M. Gisler, and D. Giardini (2006). Reconstructing the damage field of the 1855 earthquake in Switzerland: historical investigations on a well-documented event, *Geophys. J. Int.* **166**, 719–731.

Gischig, V., F. Amann, J.R. Moore, S. Loew, H. Eisenbeiss, and W. Stempfhuber (2011). Composite rock slope kinematics at the current Randa instability, Switzerland, based on remote sensing and numerical modeling, *Eng. Geol.* **118**, 37-53.

Havenith, H.-B., D. Jongmans, E. Faccioli, K. Abdrakhmatov, and P.-Y. Bard (2002). Site effect analysis around the seismically induced Ananevo rockslide, Kyrgyzstan, *Bull. Seismol. Soc. Am.* **92**, 3190-3209.

Heincke, B., Maurer, H., Green, A.G., Willenberg, H., Spillmann, T., and Burlini, L. (2006). Characterizing an unstable mountain slope using shallow 2D and 3D seismic tomography. *Geophysics* **71**, B241-B256.

Lévy, C., L. Baillet, D. Jongmans, P. Mourot, and D. Hantz (2010). Dynamic response of the Chamousset rock column (Western Alps, France), *J. Geophys. Res.* **115**, F04043, doi:10.1029/2009JF001606.

Moore, J.R., V. Gischig, E. Button, and S. Loew (2010). Rockslide deformation monitoring with fiber optic strain sensors, *Nat. Hazard Earth Sys.* **10**, 191-201.

Petley, D.N., S.A. Dunning, N.J. Rosser, and A.B. Kausar (2006). Incipient landslides in the Jhelum Valley, Pakistan following the 8th October 2005 earthquake. In: Frontiers of Science. Marui, H. Yokyo: Universal Academy Press. 47-56.

Sepúlveda, S.A., W. Murphy, R.W. Jibson, and D.N. Petley (2005). Seismically induced rock slope failures resulting from topographic amplification of strong ground motions: the case of Pacoima Canyon, California, *Eng. Geol.* **80**, 336-348.

Spillmann, T., Maurer, H., Willenberg, H., Evans, K. Heincke, B., and Green, A.G. (2007). Characterization of an unstable rock mass based on borehole logs and diverse borehole radar data. *J. Appl. Geophys.* **61**, 16-38.

Spillmann, T., H. Maurer, A.G. Green, B. Heincke, H. Willenberg, and S. Husen (2007). Microseismic investigation of an unstable mountain slope in the Swiss Alps, *J. Geophys. Res.* **112**, B07301, doi:10.1029/2006JB004723.

Spudich, P., M. Hellweg, and W.H.K. Lee (1996). Directional topographic site response at Tarzana observed in aftershocks of the 1994 Northridge, California, earthquake: implications for mainshock motions, *Bull. Seism. Soc. Am.* **86**, S193–S208.

Steidl, J.H., A.G. Tumarkin, and R.J. Archuleta (1996). What is a reference site? *Bull. Seism. Soc. Am.* **86**, 1733-1748.

Willenberg, H., S. Loew, E. Eberhardt, K. Evans, T. Spillmann, B. Heincke, H.-R. Maurer, and A. Green (2008). Internal structure and deformation of an unstable crystalline rock mass above Randa (Switzerland): Part I – Internal structure from integrated geological and geophysical investigations, *Eng. Geol.* **101**, 1-14.

Yoshimoto, K., H. Sato, S. Kinoshita, and M. Ohtake (1993). High-frequency site effect of hard rocks at Ashio, Central Japan, *J. Phys. Earth* **41**, 327-335.
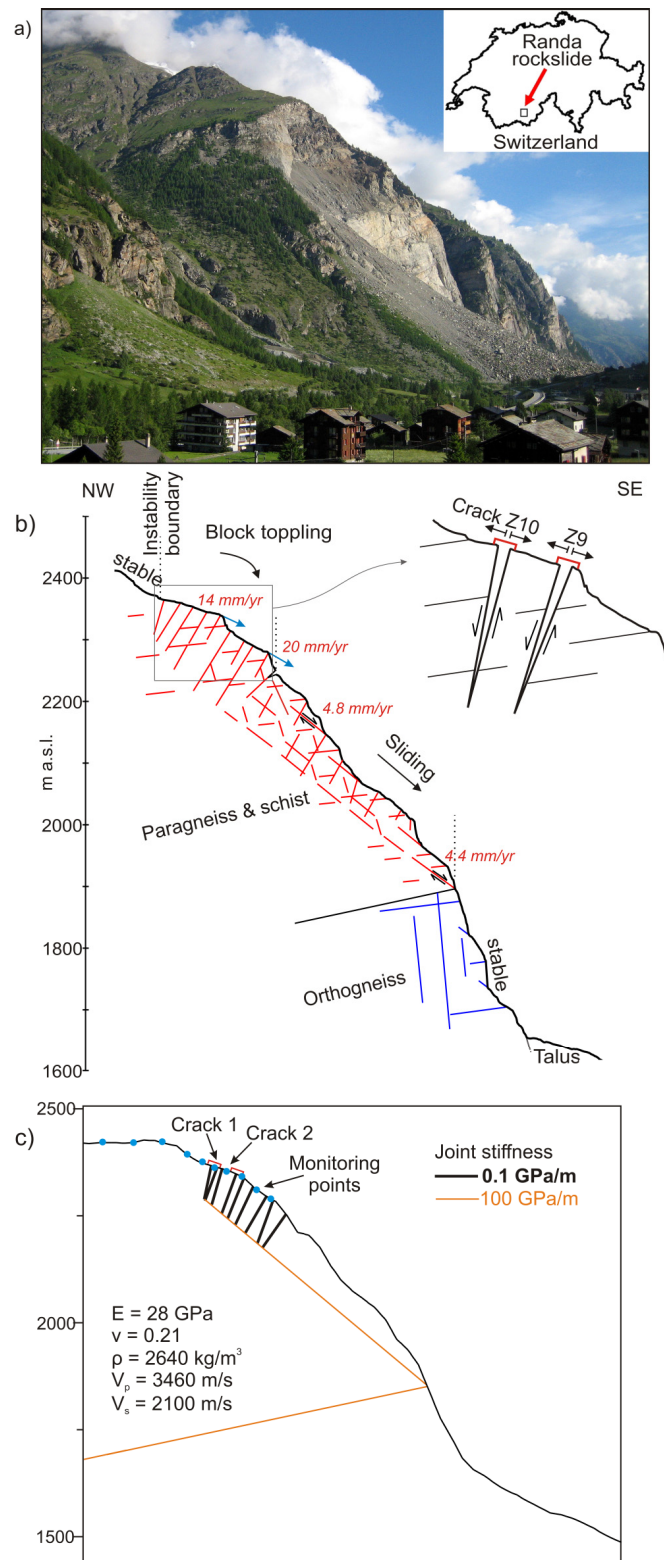
Figure 1: a) Photograph of the Randa rockslide and location within Switzerland (inset). b) Geological model of the instability from integrated measurements (adapted from *Gischig et al.,* 2011). c) Simplified model implemented in UDEC for dynamic simulation. Only steeply-dipping tension fractures mapped at the site are included and assigned low stiffness values. Monitoring points and the position of simulated crack measurements are indicated (Crack 1 ~ Z10; Crack 2 ~ Z9). Only a portion of the model is shown.
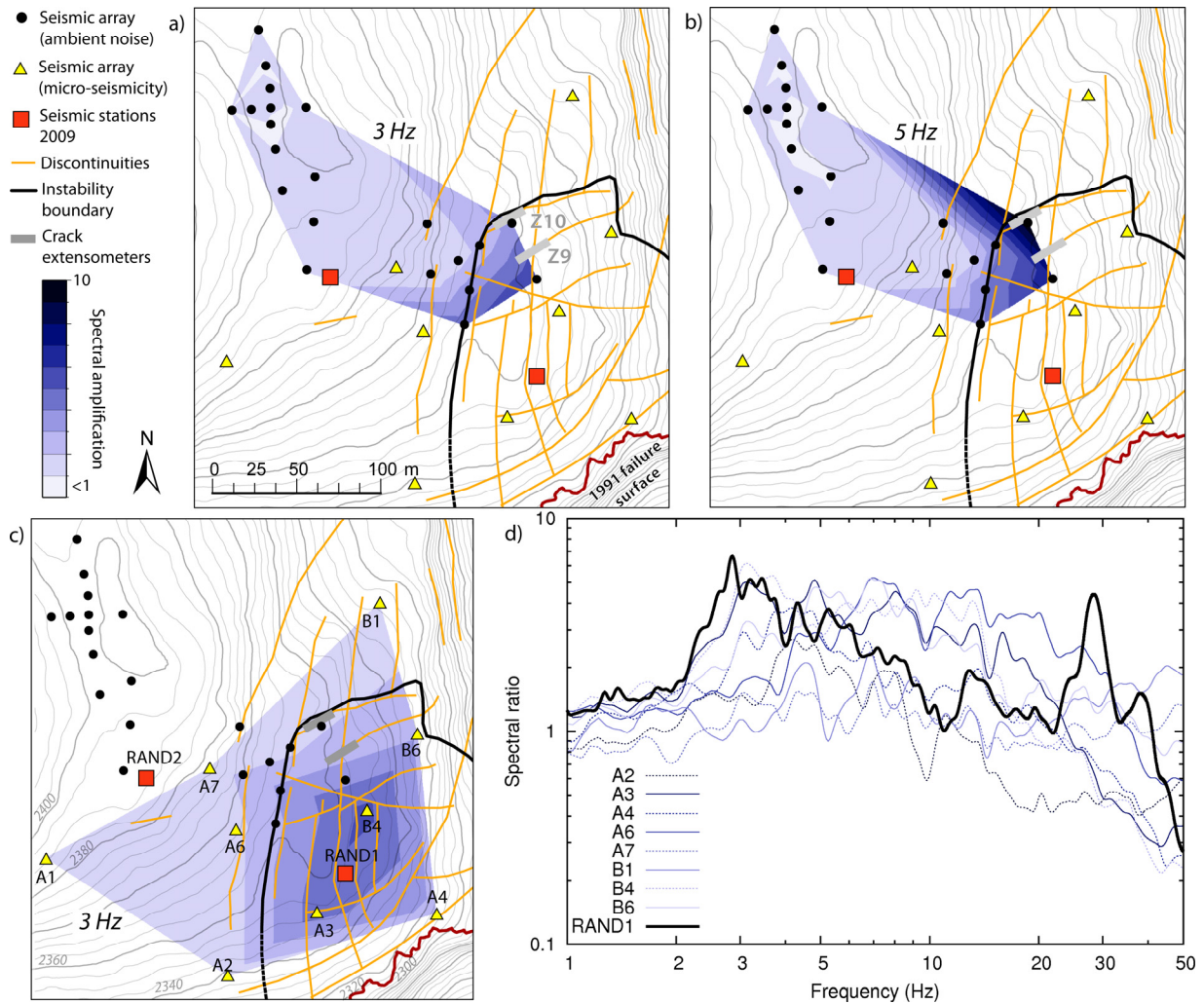
Figure 2: a) Layout of ambient noise measurements shown together with mapped and monitored discontinuities and the instability boundary. Overlain are site-to-reference spectral ratios at 3 Hz in the direction of maximum polarization (135° azimuth). b) Same as (a) for 5 Hz spectral ratios (adapted from *Burjanek et al.,* 2010). c) Overview of micro-seismic array (stations A# and B#) and seismometers (RAND1 and RAND2). Site-to-reference spectral ratios calculated from earthquake recordings are shown for 3 Hz resolved at an azimuth of 135°. d) Mean site-to-reference spectral ratios from earthquake recordings; reference for the micro-seismic array was station A1, station RAND2 served as the reference for RAND1.
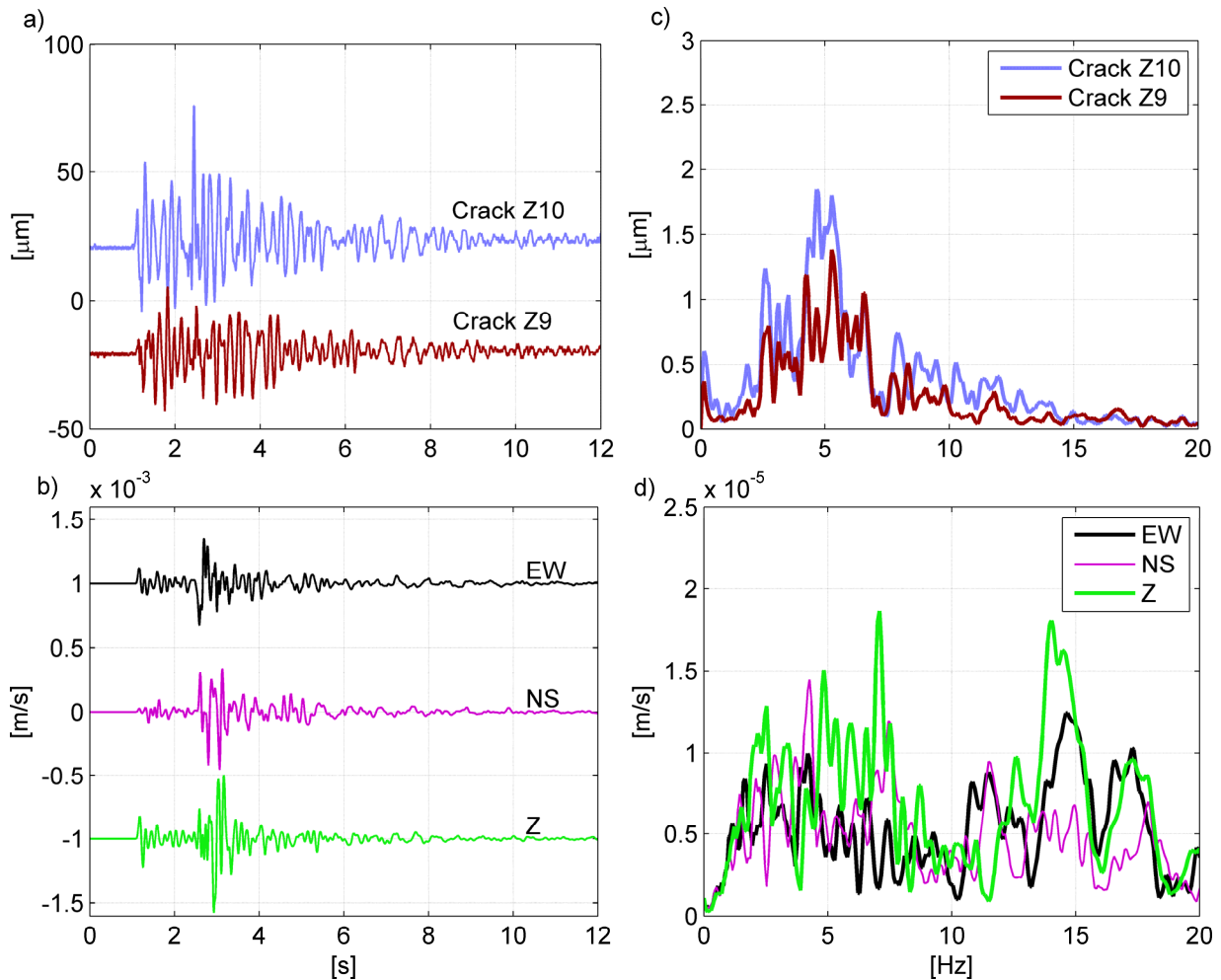
Figure 3: Ground motion data from the May 15, 2010 earthquake (M_W 3.2, source time: 05:09 UTC). a) In-situ displacement recorded by fiber optic extensometers spanning two surface tension fractures at Randa (for locations see Figure 2a). b) Seismic data from the nearest station EMBD (~5 km from epicenter). c) Spectra of fiber optic displacement data; notable are peaks at ~3 and 5 Hz. d) Spectra of ground velocity from station EMBD.
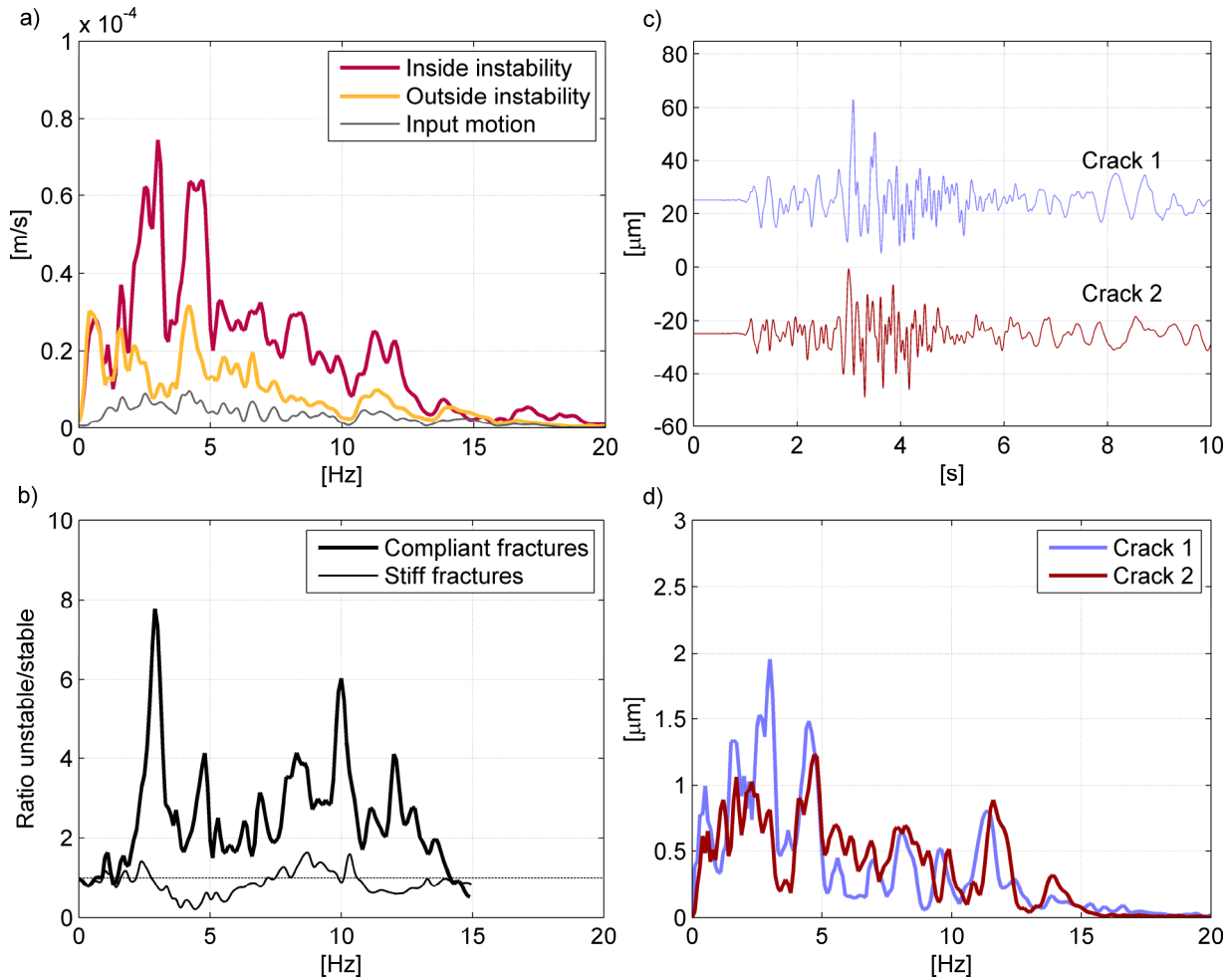
Figure 4: Simulation results: a) Mean spectra from five stations both inside and outside of the unstable area (for monitoring points see Figure 1c), together with that of the input ground motion. b) Ratio of mean spectra from (a) showing amplification within the instability with respect to adjacent stable ground; spectral ratios up to ~8 are predicted below 15 Hz. Spectral amplifications for the 'stiff' model are also shown for comparison. c) Modeled crack displacements; compare to Figure 3a. d) Spectra of modeled crack displacements; compare to Figure 3b.